Monthly Notices
of the
ROYAL ASTRONOMICAL SOCIETY

MNRAS **440,** 2013–2025 (2014) doi:10.1093/mnras/stu305

Herschel⋆-ATLAS: modelling the first strong gravitational lenses

S. Dye,[1]† M. Negrello,[2] R. Hopwood,[3] J. W. Nightingale,[1] R. S. Bussmann,[4,5] S. Amber,[6] N. Bourne,[1,7] A. Cooray,[8] A. Dariush,[3] L. Dunne,[9] S. A. Eales,[10] J. Gonzalez-Nuevo,[11] E. Ibar,[12] R. J. Ivison,[7] S. Maddox,[9] E. Valiante[10] and M. Smith[10]

[1]*School of Physics and Astronomy, Nottingham University, University Park, Nottingham NG7 2RD, UK*
[2]*INAF, Osservatorio Astronomico di Padova, Vicolo Osservatorio 5, I-35122 Padova, Italy*
[3]*Astrophysics Group, Imperial College London, Blackett Laboratory, Prince Consort Road, London SW7 2AZ, UK*
[4]*Harvard–Smithsonian Center for Astrophysics, 60 Garden St, Cambridge, MA 02138, USA*
[5]*Department of Astronomy, Space Science Building, Cornell University, Ithaca, NY 14853-6801, USA*
[6]*Department of Physical Sciences, The Open University, Walton Hall, Milton Keynes MK7 6AA, UK*
[7]*Institute for Astronomy, Royal Observatory Edinburgh, Blackford Hill, Edinburgh EH9 3HJ, UK*
[8]*Astronomy Department, California Institute of Technology, MC 249-17, 1200 East California Boulevard, Pasadena, CA 91125, USA*
[9]*Department of Physics and Astronomy, University of Canterbury, Private Bag 4800, Christchurch 8140, New Zealand*
[10]*School of Physics and Astronomy, Cardiff University, The Parade, Cardiff CF24 3AA, UK*
[11]*Instituto de Física de Cantabria (CSIC-UC), Av. los Castros s/n, 39005 Santander, Spain*
[12]*Instituto de Astrofísica, Facultad de Física, Pontificia Universidad Católica de Chile, Casilla 306, Santiago 22, Chile*

Accepted 2014 February 11. Received 2014 February 4; in original form 2013 November 27

ABSTRACT

We have determined the mass density radial profiles of the first five strong gravitational lens systems discovered by the *Herschel* Astrophysical Terahertz Large Area Survey. We present an enhancement of the semilinear lens inversion method of Warren & Dye which allows simultaneous reconstruction of several different wavebands and apply this to dual-band imaging of the lenses acquired with the *Hubble Space Telescope*. The five systems analysed here have lens redshifts which span a range $0.22 \leq z \leq 0.94$. Our findings are consistent with other studies by concluding that: (1) the logarithmic slope of the total mass density profile steepens with decreasing redshift; (2) the slope is positively correlated with the average total projected mass density of the lens contained within half the effective radius and negatively correlated with the effective radius; (3) the fraction of dark matter contained within half the effective radius increases with increasing effective radius and increases with redshift.

Key words: galaxies: evolution – galaxies: structure.

1 INTRODUCTION

Early-type galaxies, despite being relatively well studied, continue to challenge our complete understanding of their formation and evolution. Current unanswered questions include quantifying the role of mergers in their evolution (e.g. van Dokkum et al. 1999; Khochfar & Burkert 2003; Bell et al. 2006; Hilz, Naab & Ostriker 2013), reliably determining their stellar build-up and reconciling this with downsizing (e.g. Thomas et al. 2005; Maraston et al. 2009; Tojeiro et al. 2012), understanding the evolution of the upper end of the mass function (e.g. Bundy, Ellis & Conselice 2005; Bundy, Treu & Ellis 2007; van der Wel et al. 2009; Hopkins et al. 2010) and identifying the process(es) by which the high-redshift population becomes dramatically less compact at low redshifts (e.g. Daddi et al. 2005; Trujillo et al. 2006; van Dokkum et al. 2008; Lani et al. 2013). Regarding this last point, mergers have been suggested as the cause of the effect, but there is much disagreement (e.g. Hopkins et al. 2010; Oser et al. 2012). Notwithstanding these unknowns, it seems likely that common formation and evolution mechanisms are at play, given the tightness of observed relationships such as the Fundamental Plane, the correlation of black hole mass with central velocity dispersion and the near-isothermality of total mass density profiles.

Regarding the measurement of density profiles, this has recently become a very active pursuit within the field, motivated by the many scientific applications made possible. These applications include the provision of an observational benchmark for simulations of large-scale structure formation, constraining the initial mass function

⋆ *Herschel* is an ESA space observatory with science instruments provided by European-led Principal Investigator consortia and with important participation from NASA.

† E-mail: simon.dye@nottingham.ac.uk

(IMF) by comparing with stellar synthesis masses (e.g. Auger et al. 2010a; Treu et al. 2010; Barnabè et al. 2013), determining the Hubble constant from gravitational lens time delays (e.g. Tewes et al. 2013, see also the review by Jackson 2007) and cosmography (see Treu 2010b, and references therein). Other novel applications include using density profiles of strongly lensed systems embedded within a cluster or group environment as a direct probe of the larger scale gravitational potential (e.g. Dye et al. 2007; Limousin et al. 2010) and making predictions of the self-annihilation signal of dark matter to guide annihilation detection experiments (e.g. Walker et al. 2011).

A debate that continues to be rekindled is the issue of whether density profiles are cored, whereby the density tends to a constant value towards small radii or whether they are cuspy, whereby the density continues to increase as a radial power law. To the advocates of cuspy profiles, the debate is over the extent to which they are cuspy, i.e. the exponent of the radial power law. The motivation that drives these studies originates from comparing observed density profiles with those predicted by *N*-body simulations of large-scale structure formation.

Early simulations favoured cuspy profiles that are typically steeper than those inferred from observations (see, for example, de Blok & Bosma 2002, and citations to this work). However, these early studies were largely based on pure dark matter simulations which ignored the effects of baryons. Accordingly, the observational data concentrated on dwarf galaxies where baryons behave more like test particles in a dominating dark matter potential. Recent work by Cole et al. (2012) shows that cuspy dark matter profiles in simulated dwarf spheroidals results in stronger dynamical friction causing globular clusters to fall into the centres on a dynamical time-scale, in contrast to what is observed in these systems.

Simulations of large-scale structure are now beginning to incorporate baryons, but this is a highly complex task, fraught with many complicating factors such as black hole accretion and their subsequent feedback (e.g. Croton 2006; Ciotti, Ostriker & Proga 2009; Bryan et al. 2013), feedback from supernovae and cooling (see, for example, Duffy et al. 2010; Newton & Kay 2013). Understanding the interplay of baryons and dark matter is not only essential to a full comprehension of the formation and evolution of galaxies, but can also shed light on the properties of the dark matter itself, such as constraining the self-interaction cross-section of dark matter (Spergel & Steinhardt 2000; Loeb & Weiner 2011). In this regard, Lovell et al. (2012) find that the velocity profiles of satellite galaxies around the Milky Way are considerably better matched by warm dark matter density profiles than cold dark matter density profiles.

Improving the quality of observations of density profiles of galaxies, particularly the more poorly understood early types, therefore provides a much needed benchmark to assist in discrimination of the many different scenarios describing their history. Gravitational lensing offers a very powerful and yet conceptually simple approach to achieving this, independent of assumptions about the kinematical state of the deflecting mass. Whilst weak galaxy–galaxy lensing can be used to constrain density profiles, this, by necessity, must be conducted in a statistical sense (e.g. Velander et al. 2014) and provides measurements of the density profile on larger scales where the dark matter dominates. Conversely, strong galaxy–galaxy lensing is applicable on a per-galaxy basis and is sensitive to density profiles on small scales where the poorly constrained baryon physics is more dominant.

Early-type galaxies have a higher average lensing cross-section than disc galaxies (e.g. Maoz & Rix 1993) and hence strong galaxy–galaxy lens samples tend to harbour significantly more early- than late-type lenses. In this way, such samples provide a perfect opportunity to gain unique insights into the formation of early types, a fact that has inspired the culmination of several different lens samples to date. Recent strong galaxy–galaxy lens samples include the Sloan Lens ACS (SLACS) survey (Bolton et al. 2006) with 85 lenses out to a redshift of $z \simeq 0.4$ (median redshift $\simeq$0.2; Auger et al. 2009), the Strong Lensing Legacy Survey (SL2S; Cabanac et al. 2007) with a final total of 36 lenses in the range $0.2 \leq z \leq 0.8$ (median redshift $\simeq$0.5; Sonnenfeld et al. 2013), the Sloan WFC Edge-on Late-type Lens Survey (SWELLS; Treu et al. 2011) with 20 disc galaxy lenses at $z \lesssim 0.2$ (Dutton et al. 2013) and 20 lenses at $0.4 \leq z \leq 0.7$ identified in the Baryon Oscillation Spectroscopic Survey (BOSS; Eisenstein et al. 2011) which constitute the BOSS Emission-Line Lens Survey (BELLS; Brownstein et al. 2012). Regardless of their selection as lensing galaxies, both the SWELLS and the SLACS samples are found to be statistically consistent with being drawn at random from their parent unlensed samples with the same mass and redshift distributions (Bolton et al. 2008; Treu et al. 2011). This fortifies the role of lens samples in their aforementioned applications.

Analysis of these existing lens surveys has already enabled some interesting insights into galaxy evolution. For example, the fraction of dark matter within half the effective radius of early types increases with galaxy size and mass (Auger et al. 2010b; Ruff et al. 2011). Another intriguing result which has direct consequences for simulations of large-scale structure is that the total density profile of early-type galaxies appears to steepen with decreasing redshift (Ruff et al. 2011; Bolton et al. 2012; Sonnenfeld et al. 2013) although the degree to which this occurs is currently in disagreement.

In this paper, we present modelling of the first five strong galaxy–galaxy lens systems identified in the *Herschel* Astrophysical Terahertz Large Area Survey (H-ATLAS; Eales et al. 2010). The H-ATLAS is a large-area survey ($\sim$550 deg^2) conducted in five passbands in the submillimetre (submm) wavelength range $100 \lesssim \lambda \lesssim 500\,\mu$m using the *Herschel Space Observatory* (Pilbratt et al. 2010). Being a submm survey, the negative *K*-correction afforded by submm galaxies means that lensed sources are much more readily detected out to significantly greater redshifts than surveys conducted at optical wavelengths. Increasing the distance of a source increases the probability of it being lensed by intervening matter. Combining this fact with the large areal coverage of H-ATLAS results in an anticipated sample of hundreds of strong galaxy–galaxy lenses (Negrello et al. 2010; González-Nuevo et al. 2012).

Such lenses also have the advantage that their submm emission is unaffected by any dust in the lens which means that a clean view of the source is obtained. This proves particularly important when reconstructing high-resolution surface brightness maps of the high-redshift lensed source for morphological studies. Furthermore, submm galaxy number counts are steep so that strongly lensed galaxies can be straightforwardly identified with simple flux selection criteria. This simple technique has also been applied by the Herschel Multi-tiered Extragalactic Survey (HerMES; Oliver et al. 2012. See Wardlow et al. 2013, for an account of the lensing aspects of this survey) and the survey carried out at mm wavelengths by the South Pole Telescope (Carlstrom et al. 2011; Vieira et al. 2013).

The ultimate size of the H-ATLAS sample is an obvious advantage in terms of improving statistical uncertainties. However, another far more compelling benefit that arises from the negative *K*-correction in the submm is that higher redshift lensed sources are more likely to be lensed by higher redshift lenses. From an evolutionary point of view, this brings about an increase in the period over

which transformations in density profiles can be determined, back to earlier times in the Universe's history when the rate of galaxy evolution was stronger (for a theoretical perspective, see, for e.g. Schaye et al. 2010). In addition to this, almost all submm galaxies have extended structure on the scales of typical galaxy lens caustics so that their lensed images comprise extended arcs and ring-like structures. As demonstrated by Dye & Warren (2005) in application of the semilinear inversion (SLI) algorithm (Warren & Dye 2003), extended structure in lensed images allows stronger constraints to be placed on the density profile of the lensing galaxy.

In this paper, we apply an enhanced version of the SLI method which allows multiple data sets observed at different wavelengths to be simultaneously reconstructed with the same lens model. We apply this to *Hubble Space Telescope* (*HST*) images acquired in both the $F110\,W$ and $F160\,W$ filters of each of the five lenses identified in the 14.4 deg^2 data released by the H-ATLAS consortium as science demonstration phase (SDP) data.

The layout of this paper is as follows: Section 2 outlines the data. In Section 3, we describe the methodology of the lens modelling, including a description of the enhanced SLI method. Section 4 presents the results and we summarize the findings of this work in Section 6. Throughout this paper, we assume the following cosmological parameters; $H_0 = 67\,\mathrm{km\,s^{-1}\,Mpc^{-1}}$, $\Omega_\mathrm{m} = 0.32$, $\Omega_\Lambda = 0.68$ [Ade et al. (Planck Collaboration) 2013].

2 DATA

The data analysed in this work are more thoroughly described in a companion paper (Negrello et al. 2014, hereafter denoted N14) but we include the pertinent details here for completeness.

The *HST* observations were carried out in 2011 April in Cycle 18 under proposal 12194 (PI Negrello) using the Wide Field Camera 3 (WFC3). Two orbits were allocated per target with at least three quarters of the total exposure time per target of 5130 s acquired in the $F160\,W$ filter and the remainder in the $F110\,W$ filter. Images were reduced using the IRAF MULTIDRIZZLE package and resampled to a pixel scale of 0.064 arcsec, half the intrinsic pixel scale of the WFC3.

The lens galaxy flux and lensed background source image in each system were then simultaneously fitted with smooth profiles using the GALFIT software (Peng et al. 2002) and the lens profiles subtracted to leave the lensed image. These lens-subtracted images, along with their corresponding noise maps and point spread functions (PSFs) modelled by TINYTIM (Krist 1993) are those used by the SLI reconstruction algorithm.

The left-hand column in Fig. 1 shows the resulting $F110\,W$ and $F160\,W$ images for each system. We applied annular elliptical masks (after PSF convolution), fitted by eye to each image, to include only the lensed image features. This also masks any noisy residuals which remain after the GALFIT subtraction.

3 METHODOLOGY

In this paper, we apply the SLI method originally derived by Warren & Dye (2003). We use the Bayesian version of the SLI method applied by Dye et al. (2007, 2008), based on the version developed by Suyu et al. (2006). In addition, the adaptive source plane grid introduced by Dye & Warren (2005) is used.

In this section, we describe an enhancement to the SLI method that allows multiple images to be simultaneously reconstructed using the same lens mass model. Including multiple images in the inversion gives rise to stronger constraints on the lens model parameters. This is particularly true if the images are observed at different wavelengths since colour variations across the lensed source mean that each image probes a different line of sight through the gravitational potential of the lensing galaxy. We describe the modifications necessary for the inclusion of multiple images but refer the reader to the aforementioned papers for more comprehensive details of the underlying SLI method.

3.1 Multi-image SLI method

The SLI method assumes a pixelized image and a pixelized source plane. For a given lens model, the method computes the linear superposition of lensed images of each source plane pixel that best fits the observed lensed image. In the original formulation, the rectangular matrix f_{ij} held the fluxes of lensed image pixels j for each source plane pixel i of unit surface brightness. In this way, a model lensed image was created with flux values equal to $\sum_i s_i f_{ij}$ for each image pixel j given source pixel surface brightnesses s_i. Subtracting this model image from the observed image, which has pixel flux values d_j and 1σ uncertainties σ_j, allows the χ^2 statistic to be computed.

To cope with multiple images, we need to introduce a new index to each of these quantities to denote separate image numbers. The χ^2 statistic in this case becomes

$$\chi^2 = \sum_{k=1}^{K} \left[\sum_{j=1}^{J_k} \left(\frac{\sum_{i=1}^{I_k} s_i^k f_{ij}^k - d_j^k}{\sigma_j^k} \right)^2 \right], \tag{1}$$

where there is now an additional sum over images k. Note that each image k has its own source image with surface brightnesses s_i^k in pixels i. The image of each of these pixels stored in f_{ij}^k must be convolved with the PSF of the observed image k. Also note that each of the k sources and k images can have different numbers of pixels, I_k and J_k, respectively.

As in the single-image version of the SLI method, the minimum χ^2 solution is given by

$$\boldsymbol{s} = \mathbf{F}^{-1}\boldsymbol{d} \tag{2}$$

but now the matrix $\mathbf{F}$ is a block-diagonal matrix diag($\mathbf{F}^1$, $\mathbf{F}^2$, ..., $\mathbf{F}^K$) comprising the submatrices $\mathbf{F}^k$ and $\boldsymbol{d}$ is a column vector which itself has column vector elements $\boldsymbol{d}^k$. The elements of $\mathbf{F}^k$ and $\boldsymbol{d}^k$ are, respectively,

$$F_{ij}^k = \sum_{n=1}^{J_n} f_{\mathrm{in}}^k f_{jn}^k / (\sigma_n^k)^2 \,, \quad d_i^k = \sum_{n=1}^{J_n} f_{\mathrm{in}}^k d_n^k / (\sigma_n^k)^2 \,. \tag{3}$$

Finally, the column vector $\boldsymbol{s}$ contains the source pixel surface brightnesses arranged in order $s_1^1, s_2^1, \ldots, s_{I_1}^1, s_1^2, \ldots, s_{I_K-1}^K, s_{I_K}^K$.

To regularize the solution, equation (2) must be modified by the regularization matrix $\mathbf{H}$ as described in Warren & Dye (2003). However, in the case of multiple images, $\mathbf{H}$ becomes the block diagonal matrix diag($\lambda_1\mathbf{H}^1, \lambda_2\mathbf{H}^2, \ldots, \lambda_K\mathbf{H}^K$), where each submatrix $\mathbf{H}^k$ corresponds to the chosen regularization matrix for source k. Note that in this formalism, each source k is assigned its own independent regularization weight λ_k. We regularize each source plane using the scheme described in Dye et al. (2008) appropriate for adaptive source grids. In principle, instead of regularizing each source plane independently, different source planes could be allowed to regularize one another in which case $\mathbf{H}$ would not be block-diagonal. This could be beneficial if the source is expected to be similar between the different input images but would bias the lens model if not.

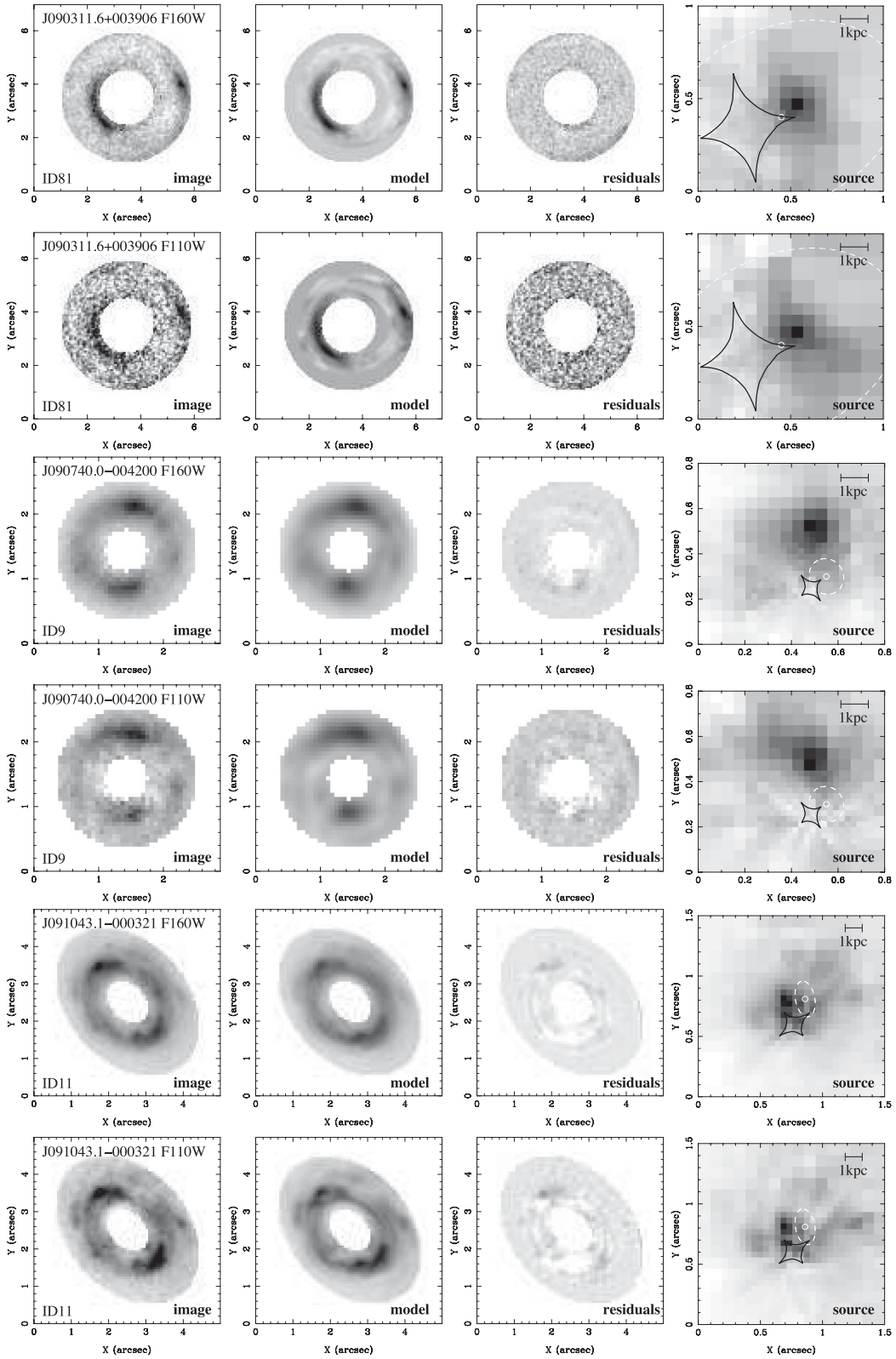

Figure 1. Lens reconstructions. Reading from left to right, columns show the observed image (masked and lens subtracted), the model image, the residuals (observed image minus model; grey-scale same as corresponding images) and reconstructed source surface brightness map (the solid black or white line shows the caustic and the dashed white line and small circle, respectively, show the source half-light area and source centre obtained by B13 at 880 μm). For each system, the $F110\,W$ and $F160\,W$ data are shown. In all panels, north points along the positive y-axis and west points along the positive x-axis.

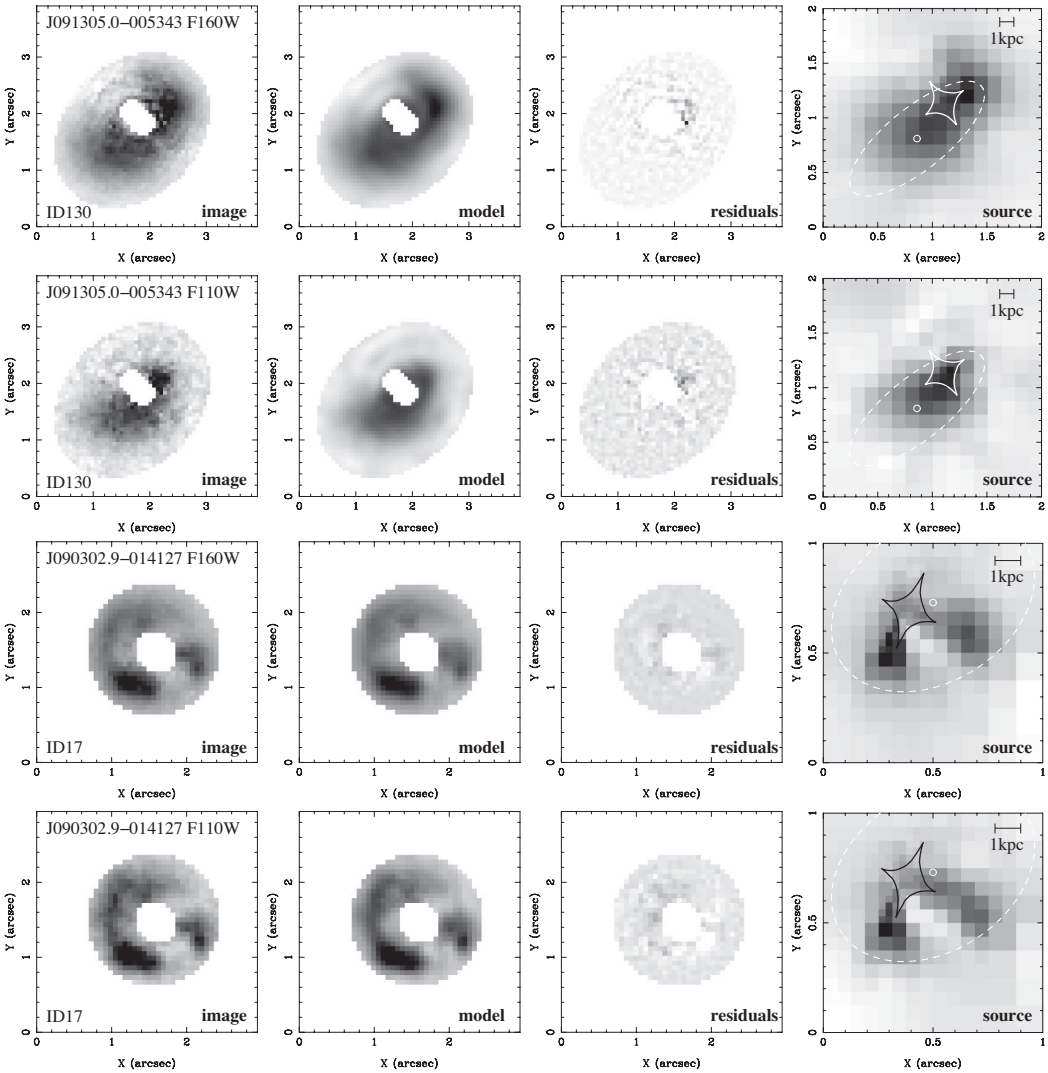

Figure 1 – *continued*

The procedure for finding the most probable lens model parameters then turns to Bayesian inference as described by Dye et al. (2008). Adapting equation 7 in Dye et al. (2008) to the multi-image case here results in the following expression for the Bayesian evidence, ϵ:

$$-2\ln\epsilon = \chi^2 + \ln\left[\det(\mathbf{F}+\mathbf{H})\right] - \ln\left[\det(\mathbf{H})\right] + \boldsymbol{s}^{\mathrm{T}}\mathbf{H}\boldsymbol{s} + \sum_{k=1}^{K}\sum_{j=1}^{J_k}\ln\left[2\pi(\sigma_j^k)^2\right] \quad (4)$$

with χ^2 given by equation (1) and where $\mathbf{F}$, $\mathbf{H}$ and $\boldsymbol{s}$ are the multi-image quantities defined above. The negative logarithm of the evidence as given above is then minimized by applying the Markov Chain Monte Carlo (MCMC) technique to the lens model parameters (see the next section), the regularization weights[1] and a parameter called the 'splitting factor' which controls the distribution of source plane pixel sizes on the adaptive grid (see Dye et al. 2008, for more details). After the MCMC chain has burnt in, we allow a further 100 000 iterations to estimate parameter confidences.

[1] In practice, we have opted to set the same regularization weight across all images to simplify the MCMC minimization.

We note a further practicality. When computing the χ^2 term in equation (4), we carry out the sum over image pixels contained within an annular mask surrounding the ring. The mask is tailored for each image to include the image of the entire source plane, with minimal extraneous sky. This increases the fraction of significant image pixels with the effect that the evidence is more sensitive to the model parameters.

Finally, we point out that the multi-image SLI method as presented assumes that all images are statistically independent of each other. In the case of images that are not statistically independent, for example, as could be the case with image slices in an integral field unit data cube or spectral-line interferometric data cube, equation (1) must be modified to include the relevant covariance terms.

3.2 Lens model

We model each of the five lenses considered in this work with a single smooth density profile to describe the distribution of the total (baryonic and dark) lens mass. In order to directly compare with the work of Bolton et al. (2012) and Sonnenfeld et al. (2013), we use the power-law density profile assumed in these studies. The volume mass density of this profile, ρ, scales with radius, r, as

$\rho \propto r^{-\alpha}$. The implicit assumption made with this profile is that the power-law slope, α, is scale invariant. This assumption appears to be reasonable, at least on the scales probed by strong lensing, since there is no apparent trend in slope with the ratio of Einstein radius to effective radius (Koopmans et al. 2006; Ruff et al. 2011).

The corresponding projected mass density profile we therefore use in the lens modelling is the elliptical power-law profile introduced by Kassiola & Kovner (1993), which has a surface mass density, κ, given by

$$\kappa = \kappa_0 \, (\tilde{r}/1\,\mathrm{kpc})^{1-\alpha} \, , \tag{5}$$

where κ_0 is the normalization surface mass density (the special case of $\alpha = 2$ corresponds to the singular isothermal ellipsoid). The radius $\tilde{r}$ is the elliptical radius defined by $\tilde{r}^2 = x'^2 + y'^2/\epsilon^2$, where ϵ is the lens elongation defined as the ratio of the semimajor to semiminor axes. There are three further parameters that describe this profile: the orientation of the semimajor axis measured in a counterclockwise sense from north, θ, and the coordinates of the centre of the lens in the image plane, (x_c, y_c). We also include two further parameters to allow for an external shear field, namely, the shear strength, γ, and shear direction angle, again measured counterclockwise from north, θ_γ. The shear direction angle is defined to be perpendicular to the direction of resulting image stretch. This brings the total number of lens model parameters to eight. We assume a uniform prior for all eight parameters. In the MCMC contour plots presented in the appendix, we marginalize over (x_c, y_c) since we did not detect any significant offsets between the lens mass centre and the centroid of the lens galaxy light.

4 RESULTS

The reconstruction of each of the five lenses is shown in Fig. 1. Table 1 gives the lens model parameters, including the geometric average Einstein radius, θ_E, computed as

$$\left(\frac{\theta_E}{1\,\mathrm{kpc}}\right) = \left(\frac{2}{3-\alpha}\,\frac{1}{\sqrt{\epsilon}}\,\frac{\kappa_o}{\Sigma_{CR}}\right)^{\frac{1}{\alpha-1}} , \tag{6}$$

where Σ_{CR} is the critical surface mass density (see, for example Schneider, Ehlers & Falco 1992).

4.1 Object notes

In this section, we detail the characteristics of each lens system. In particular, we compare with the results of Bussmann et al. (2013, B13 hereafter) who have modelled imaging data acquired with the Submillimeter Array (SMA) for ∼30 candidate lenses discovered by H-ATLAS and HerMES. All five of the H-ATLAS SDP lenses are modelled by B13, although we point out that external shear is not included in their lens model.

J090311.6+003906 (ID81). This is a classic cusp–caustic configuration lens. The near-IR emission in the lensed image closely matches that of the SMA data and unsurprisingly results in a consistent magnification. The reconstructed source in both *HST* filters shows little structure other than a slight elongation along the NE–SW direction. The centroid of the source is well aligned with that found by B13. The lens model is an excellent fit to the observed data and leaves no significant residuals. The model requires a small amount of external shear with strength $\gamma \simeq 0.05$ and direction $\theta_\gamma \simeq 105^\circ$, consistent with perturbations expected from a nearby group of galaxies to the east. The elongation and orientation of the required model is entirely consistent with that of the observed light profile.

J090740.0−004200 (ID9). This lens system is dominated by a single doubly imaged source with a simple morphology lying to the north of the lens galaxy centroid. The double imaging is consistent with the SMA data but the emission appears to originate from a different location in the source compared to what is observed in the near-IR *HST* data. The reconstructed source $F110\,W$–$F160\,W$ colour map shows a reddening gradient which points from the near-IR source towards the SMA source centroid. Some of the fainter emission from the source in the near-IR crosses the caustic and gives rise to the observed complete Einstein ring. There is also some fainter structure in the ring which is fit in the model by a fainter source to the east of the lens centroid. Negligible external shear is required in the best-fitting lens model. The modest elongation of $\epsilon = 1.14$ indicates a more radially symmetric mass profile compared to the light. The mass and light are significantly misaligned in this lens (see Section 4.4).

J091043.1−000321 (ID11). Like ID9, this system has a complete Einstein ring. The ring's significant ellipticity is the result of a relatively strong external shear field of strength $\gamma = 0.23$. The direction of this shear points almost exactly to the centre of a nearby edge-on spiral galaxy to the NW located at a redshift of $z = 0.39 \pm 0.09$ (see N14). The implication is therefore that this spiral is almost entirely responsible for the shear perturbation. We attempted a model where external shear was replaced by a second singular isothermal lens to represent the spiral's total mass but found no significant improvement in the fit. The reconstructed source exhibits clear small-scale structure in both filters, required to fit the observed structure in the ring. The majority of the emission observed in the ring comes from a doubly imaged source lying just outside the caustic and the smaller scale structure comes from smaller knots of emission in the source, some of which are quadruply imaged. As the residual plot in Fig. 1 indicates, the model image does not perfectly account for the observed features in the ring and this is also reflected in the fact that the model fit is only marginally acceptable. It is therefore

Table 1. Lens model parameters. Reading from left to right, columns are the H-ATLAS identifier (including the Negrello et al. 2010 identifier), the lens redshift, z_d, the source redshift, z_s, the density profile slope, α, the lens mass normalization, κ_0 (in units of 10^{10} $M_\odot$ kpc^{-2}), the elongation of the lens mass profile, ϵ, the orientation of the semimajor axis of the lens, θ, measured counterclockwise from north, the strength of the external shear component, γ, and the Einstein radius, θ_E, in arcsec computed from equation (6).

ID	z_d	z_s	α	κ_0	ϵ	$\theta(^\circ)$	γ	θ_E(arcsec)
J090311.6+003906 (ID81)	0.2999	3.042	$1.93^{+0.06}_{-0.06}$	$0.81^{+0.03}_{-0.03}$	$1.27^{+0.07}_{-0.07}$	11^{+8}_{-6}	$0.04^{+0.02}_{-0.01}$	1.56 ± 0.11
J090740.0−004200 (ID9)	0.6129	1.577	$1.96^{+0.05}_{-0.07}$	$0.60^{+0.02}_{-0.02}$	$1.14^{+0.08}_{-0.08}$	43^{+3}_{-3}	$0.01^{+0.01}_{-0.01}$	0.71 ± 0.05
J091043.1−000321 (ID11)	0.7932	1.786	$1.80^{+0.05}_{-0.04}$	$0.76^{+0.02}_{-0.02}$	$1.37^{+0.05}_{-0.04}$	46^{+3}_{-3}	$0.23^{+0.01}_{-0.01}$	0.84 ± 0.04
J091305.0−005343 (ID130)	0.2201	2.626	$1.74^{+0.20}_{-0.24}$	$0.26^{+0.02}_{-0.02}$	$1.34^{+0.18}_{-0.15}$	54^{+14}_{-10}	$0.02^{+0.02}_{-0.02}$	0.43 ± 0.08
J090302.9−014127 (ID17)	0.9435	2.305	$1.37^{+0.21}_{-0.20}$	$0.31^{+0.04}_{-0.04}$	$1.29^{+0.15}_{-0.17}$	149^{+19}_{-26}	$0.03^{+0.03}_{-0.03}$	0.36 ± 0.06

possible that some of the ring structure is actually structure in the lens galaxy not fully removed by GALFIT. The SMA data imply a doubly imaged source which, like J090740.0−004200, is offset from the near-IR emission but has a comparable Einstein radius. As with ID9, the reconstructed source $F110\,W$–$F160\,W$ colour map shows a reddening gradient which points from the near-IR source towards the SMA source centroid.

In addition to the reconstructed near-IR source presented here, there appears to be further lensed arcs associated with this system (not shown in Fig. 1). Two readily identified arcs lie to the south and to the east of the lens centre and trace out a ring with an Einstein radius larger than that shown in Fig. 1. This implies that the lensed source responsible lies at a different redshift. We chose not to complicate the lens model further by incorporating this additional source but instead leave this for further work.

J091305.0−005343 (ID130). The lens galaxy is relatively poorly constrained in this system. The best-fitting model is consistent with zero external shear (as might be expected from the lack of observed nearby perturbers) and the lens has one of the higher elongations found in the sample of $\epsilon = 1.34$. The best-fitting reconstructed source is very extended and as such, the magnification is low. The residual map shown in Fig. 1 shows some significant features towards the lens centre which is not surprising given the difficulty reported by N14 in removing the lens light. However, the residuals contribute an insignificant amount of light to the overall source and as such will have a negligible effect on the lens model parameters. The SMA data are in close agreement with the near-IR data which increases confidence in the GALFIT subtraction (see N14), although the near-IR data imply a slightly larger magnification than the SMA data. We make the caveat that this lens, as pointed out by N14, is a likely Sa galaxy. In order to compare our results with those of the aforementioned lensing studies which include only early-type lenses, we have omitted this system from our fits to the trends reported later in this paper.

J090302.9−014127 (ID17). This is a relatively poorly constrained lens although the fit is acceptable. There are some minor features in the residual image which occur at 3 o'clock and 11 o'clock around the inner radius of the annulus as shown in Fig. 1. N14 have modelled the flux in the lensed image by fitting individual GALFIT profiles to the different components. Two of these profiles lie on the inner radius of the annulus and these coincide with the locations of the residuals found in the lens modelling here. One interpretation is therefore that spatially dependent extinction in the lensing galaxy affects the lensed image. This is consistent with the colour of the feature at 11 o'clock which N14 determine as having a significantly redder colour than the average colour of the other GALFIT profiles, but not with the feature at 3 o'clock which is consistent in colour. An alternative explanation might therefore be that the lensed image contains residual flux from the lensing galaxy itself which is highly possible given the complexity in removing the lens from this system. Nevertheless, the reconstructed source plane shows two very prominent elongated objects in both bands which converge at a point interior to the caustic. The majority of this source plane emission is doubly imaged but some of the flux in the merged region is quadruply imaged. The fact that the lensed image is well fitted by a relatively simple source surface brightness map adds reassurance that the reconstruction is plausible; an over-complicated source often indicates that there are non-lensed features in the lensed image. Although the SMA data for this lens are unable to resolve individual ring features, B13 obtain a magnification consistent with that measured from the near-IR data here.

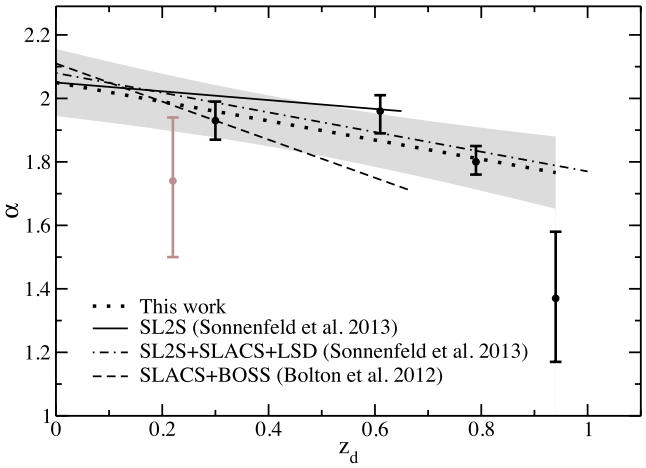

Figure 2. Variation of the density profile slope, α, as a function of the lens redshift, z_d. The solid and dashed lines show the redshift dependence of α using the SL2S lenses by Sonnenfeld et al. (2013) and the SLACS + BELLS lenses by Bolton et al. (2012), respectively. The extent of each line indicates the extent of the lens redshifts in the respective surveys. The grey data point corresponds to the Sa lens J091305.0−005343 which has been excluded in our fit shown by the dotted line and grey shaded 1σ error envelope.

4.2 Mass profile versus redshift

Fig. 2 shows the fitted lens density profile slopes plotted against redshift. Discounting the likely Sa lens J091305.0−005343, the straight line minimum χ^2 fit through the four data points is $\alpha = 2.05 \pm 0.08 - (0.30 \pm 0.13)z$. (If we include this fifth lens, the fit becomes $\alpha = 2.01 \pm 0.10 - (0.25 \pm 0.15)z$.) The dotted line and grey shaded envelope in Fig. 2 shows the fit and the 1σ error region, respectively. In the same figure, we plot the variation in slope with redshift from three other lens sample combinations: (1) the SL2S lens sample of $\alpha = 2.05 \pm 0.06 - (0.13 \pm 0.24)z$ from Sonnenfeld et al. (2013), (2) the combination of the Lensing Structure and Dynamics sample of Treu & Koopmans (2004), SL2S and SLACS of $\alpha = 2.08 \pm 0.02 - (0.31 \pm 0.10)z$ also from Sonnenfeld et al. (2013) and (3) the combination of SLACS and BOSS of $\alpha = 2.11 \pm 0.02 - (0.60 \pm 0.15)z$ from Bolton et al. (2012).

As is apparent from Fig. 2, our inferred rate of change in slope with redshift is not inconsistent with that measured by any of the other studies plotted in the figure, although neither is it inconsistent with a null rate of change. This is perhaps not surprising given the small sample size presently at our disposal. This limitation will be considerably reduced by our forthcoming rapidly growing lens sample.

4.3 Lens magnifications

Table 2 lists the source flux magnifications. For each lens, we have computed the magnification at every point in the MCMC chain as presented in Fig. A1 to form a magnification distribution. Table 2 then quotes the median magnification and its ±34 per cent bounds.

We computed magnifications using the higher signal-to-noise $F160\,W$ data to give more precise magnifications. We find that the magnifications computed using the $F110\,W$ data generally have a larger spread but the distribution is always consistent with those computed using the $F160\,W$ data.

We determined three different magnifications to give an indication of the strength of near-IR differential amplification. The first is

Table 2. Source flux magnifications. The quantities listed are: the total source flux magnification, $\mu_{\rm tot}$; the magnifications, $\mu_{0.5}$ and $\mu_{0.1}$ which give the magnification of the brightest region(s) of the source, respectively, contributing 50 and 10 per cent of the total reconstructed source flux; the magnification at 880 μm, μ_{880}, computed by B13 for an area of the source which is four times the source's half-light area.

ID	$\mu_{\rm tot}$	$\mu_{0.5}$	$\mu_{0.1}$	μ_{880}
J090311.6+003906 (ID81)	$10.6^{+0.6}_{-0.7}$	$13.8^{+1.0}_{-0.9}$	$21.0^{+1.6}_{-1.4}$	11.1 ± 1.1
J090740.0−004200 (ID9)	$6.29^{+0.27}_{-0.26}$	$7.23^{+0.31}_{-0.34}$	$5.80^{+0.38}_{-0.27}$	8.8 ± 2.2
J091043.1−000321 (ID11)	$7.89^{+0.21}_{-0.25}$	$12.5^{+0.40}_{-0.43}$	$28.3^{+2.1}_{-3.5}$	10.9 ± 1.3
J091305.0−005343 (ID130)	$3.09^{+0.22}_{-0.21}$	$4.01^{+0.25}_{-0.25}$	$7.51^{+0.32}_{-0.37}$	2.1 ± 0.3
J090302.9−014127 (ID17)	$3.56^{+0.19}_{-0.17}$	$4.48^{+0.33}_{-0.25}$	$5.54^{+0.41}_{-0.30}$	4.9 ± 0.7

Table 3. Morphology of the lens light profile and lens masses. Columns are: elongation, $\epsilon_{\rm light}$, position angle (measured counter-clockwise from north), $\theta_{\rm light}$, effective radius, $R_{\rm e}$, the stellar mass contained within a radius of $R_{\rm e}/2$ for a Salpeter and Chabrier IMF, $M^{*,\rm Salp}_{R_{\rm e}/2}$ and $M^{*,\rm Chab}_{R_{\rm e}/2}$, respectively (derived from the stellar masses computed in N14) and the total mass within a radius of $R_{\rm e}/2$ inferred from the lens model, $M^{\rm Tot}_{R_{\rm e}/2}$. All masses are in units of $10^{10}\,{\rm M}_{\odot}$. Note that the light profile parameters for J091305.0−005343 refer only to the bulge component and exclude the faint disc.

ID	$\epsilon_{\rm light}$	$\theta_{\rm light}(^{\circ})$	$R_{\rm e}$ (arcsec)	$R_{\rm e}$ (kpc)	$M^{*,\rm Salp}_{R_{\rm e}/2}$	$M^{*,\rm Chab}_{R_{\rm e}/2}$	$M^{\rm Tot}_{R_{\rm e}/2}$
J090311.6+003906 (ID81)	1.24 ± 0.01	10 ± 1	0.45	2.1	4.36 ± 1.30	2.45 ± 0.73	6.46 ± 0.24
J090740.0−004200 (ID9)	1.31 ± 0.01	59 ± 1	0.41	2.9	3.56 ± 1.07	2.00 ± 0.60	6.17 ± 0.21
J091043.1−000321 (ID11)	1.58 ± 0.01	21 ± 2	0.38	3.0	4.08 ± 2.92	2.29 ± 1.64	8.91 ± 0.23
J091305.0−005343 (ID130)	1.18 ± 0.02	43 ± 4	0.31	1.2	2.14 ± 0.62	1.20 ± 0.35	1.26 ± 0.10
J090302.9−014127 (ID17)	1.79 ± 0.01	16 ± 2	0.40	3.2	1.55 ± 0.59	0.87 ± 0.33	3.31 ± 0.42

a 'total magnification', $\mu_{\rm tot}$, computed as the ratio of the total flux in the masked region of the image as shown in Fig. 1 to the total flux in the source plane. The second and third, $\mu_{0.5}$ and $\mu_{0.1}$, correspond to the magnification of the brightest region(s) of the source that contributes 50 and 10 per cent, respectively, of the total reconstructed source flux. Note that $\mu_{\rm tot}$ is almost always lower than $\mu_{0.5}$ and $\mu_{0.1}$ since incorporating the total source plane typically includes additional regions that are less magnified.

Table 2 also lists the magnifications, μ_{880}, determined by B13 at 880 μm. These magnifications are calculated in an elliptical disc centred on the best-fitting 880 μm source brightness profile with a radius twice that containing half of the total source flux. μ_{880} is the ratio of the integrated flux within the image plane region mapped by this disc to the integrated flux within the disc in the source plane itself. For the Sérsic profiles fit to the SDP sources by B13, this corresponds to approximately 75 per cent of the source light in all cases. Therefore, μ_{880} corresponds to a magnification somewhere between $\mu_{\rm tot}$ and $\mu_{0.5}$.

As Table 2 shows, for all lenses apart from J091305.0−005343, μ_{880} is consistent with a value spanned by $\mu_{\rm tot}$ and $\mu_{0.5}$. The consistency is generally better when the 880 μm source morphology more closely resembles the reconstructed near-IR source. This is a reflection of the fact that the lens models determined at both wavelengths are geometrically similar.[2] The exception is J091305.0−005343 which has a very similar source morphology between 880 μm and the near-IR, but in this case, the magnification discrepancy is brought about by a significantly different lens elongation, with the near-IR lens model favouring an elongation of ∼1.3 compared to ∼2.0 at 880 μm.

[2] We note that the lens elongations derived by B13 are consistently higher than those derived in our study and we attribute this, at least partly, to the lack of external shear in the B13 lens model.

4.4 Comparison of mass and light morphology

A question which brings insight to models of galaxy formation and evolution is how closely the visible mass traces the dark matter halo. One way to address this is to compare the visible morphology of the lens galaxies to the total mass profiles determined through lensing.

We used the GALFIT models of N14 to determine the elongation and orientation of the lens galaxy surface brightness profiles. Table 3 lists these along with the effective radii. In the case of J091305.0−005343 (ID130), we used only the light profiles which make up the bulge, since the bulge comprises nearly all of the light and, unlike the faint disc, has a coherent set of profiles which give a well-defined orientation and elongation.

Fig. 3 plots the comparison of mass and light profile parameters. The top panel shows the comparison of elongations. For all five of the lenses, the total lens mass model has or is consistent with a lower elongation than that of the light. This implies that the dark matter halo is comparable in elongation or rounder in each case.

The bottom panel of Fig. 3 compares the offset in orientation of the lens mass and light profiles. Here, there are some significant discrepancies. The offsets are substantially higher on average than those found by SLACS, who measured an rms scatter of 10° (Koopmans et al. 2006), but consistent with the findings of SL2S (Gavazzi et al. 2012) who measure an rms scatter of 25° with offsets of up to 50°. As Gavazzi et al. (2012) point out, the SL2S lenses have a higher average ratio of Einstein radius to effective radius than the SLACS lenses, and hence, the SLACS lenses are more dominated by the stellar component. The average of this ratio for our lenses is even higher than that of the SL2S sample and so we would expect even less alignment between the dark and visible components. We will be able to explore this trend more properly with our forthcoming larger lens sample, although there are already indications from simulations that such large (and even larger) morphological differences between baryons and dark matter are commonplace (for example, see Bett et al. 2010; Skibba & Macciò 2011).

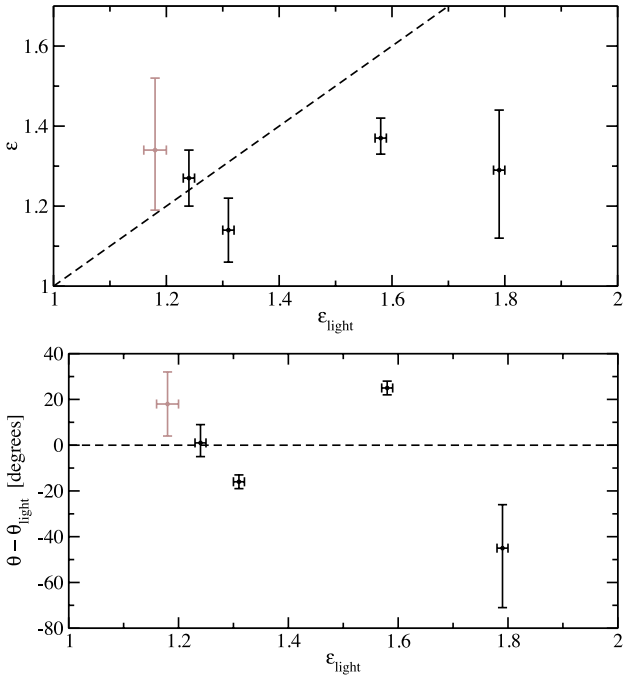

Figure 3. Comparison of light with mass. *Top panel*: elongation of lens mass profile versus elongation of observed light. *Bottom panel*: difference in position angle of lens profile and observed light versus elongation of observed light. In both panels, the grey data point corresponds to the Sa lens J091305.0−005343.

4.5 Other observational trends

An important observational benchmark for models of galaxy and structure formation is the fraction of dark matter contained within a fixed fraction of the effective radius. Using the SLACS lens sample, Auger et al. (2010b) measure an average projected fraction of dark matter within half the effective radius of 0.21 with a scatter of 0.20, for a Salpeter (1955) IMF, or 0.55 with a scatter of 0.11 for a Chabrier (2003) IMF. Ruff et al. (2011) measure the average of this fraction to be 0.42 with a scatter of 0.20 for a Salpeter IMF for the SL2S lenses.

Table 3 lists the stellar masses and the total lensing projected mass contained within half the effective radius for our lenses. To obtain these stellar masses, we used the total stellar masses and the GALFIT profiles determined for the lens galaxies by N14. Excluding the Sa lens J091305.0−005343, our lenses have a mean projected dark matter fraction within half the effective radius of $f_{\rm DM} = 0.46$ with a scatter of 0.10, for a Salpeter IMF, ($f_{\rm DM} = 0.69$ with a scatter of 0.07, for a Chabrier IMF). Although this is statistically consistent with the SLACS and SL2S lenses, the higher value measured in both our lenses and the SL2S lenses compared to the SLACS sample most likely reflects the lower average ratio of Einstein radius to effective radius in SLACS.

One of the trends detected by the SLACS survey is that $f_{\rm DM}$ for early types increases with galaxy mass and galaxy size. Auger et al. (2010b) measure the linear fit $f_{\rm DM} = -0.13 \pm 0.09 + (0.49 \pm 0.10)\log(R_{\rm e}/1\,{\rm kpc})$. However, this result is not confirmed by the SL2S lens sample; Ruff et al. (2011) fail to find any correlation between $f_{\rm DM}$ and $R_{\rm e}$ with a measured gradient of $\mathrm{d}f_{\rm DM}/\mathrm{d}R_{\rm e} = 0.08^{+0.10}_{-0.08}$ kpc^{-1}. Our lens sample, excluding the Sa lens J091305.0−005343 gives a linear fit of $f_{\rm DM} = -0.01 \pm 0.20 + (1.04 \pm 0.46)\log(R_{\rm e}/1\,{\rm kpc})$, steeper but consistent with the SLACS lenses.

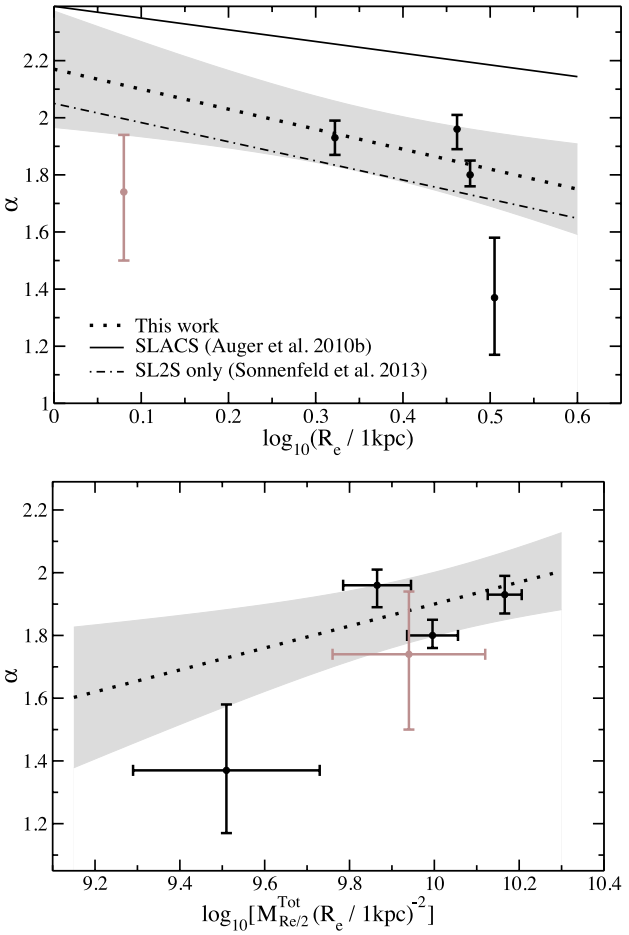

Figure 4. Correlation between total mass density profile slope, α, and effective radius, $R_{\rm e}$, (*top panel*) and average projected total surface mass density within $R_{\rm e}/2$ (*bottom panel*). In both panels, the Sa lens J091305.0−005343, coloured with a grey data point, has been omitted in the straight line fit which is shown by the dotted line and grey shaded 1σ error envelope.

The SLACS and SL2S lenses also exhibit the trend that the slope of the density profile inferred from lensing is negatively correlated with effective radius and positively correlated with the average surface mass density contained within $R_{\rm e}/2$. In Fig. 4, we plot these correlations for our lenses. The top panel shows the density profile slope, α, plotted against effective radius. For our four early-type lenses, we obtain a straight line fit of $\alpha = 2.17 \pm 0.20 - (0.70 \pm 0.47)\log(R_{\rm e}/1\,{\rm kpc})$, as shown in the figure by the dotted line and grey shaded 1σ error envelope. This compares to the fit $\alpha = 2.39 \pm 0.10 - (0.41 \pm 0.12)\log(R_{\rm e}/1\,{\rm kpc})$ by Auger et al. (2010b) for the SLACS lenses and $\alpha = 2.05 \pm 0.06 - (0.67 \pm 0.20)\log(R_{\rm e}/1\,{\rm kpc})$ by Sonnenfeld et al. (2013) for the SL2S lenses.[3]

In the bottom panel of Fig. 4, we plot α against the average total surface mass density within half the effective radius, as quantified by the ratio $M^{\rm Tot}{}_{R_{\rm e}/2}/(R_{\rm e}/1\,{\rm kpc})^2$. We obtain a straight line fit of $\alpha = 11.60 \pm 0.11 + (0.35 \pm 0.22)\log(M^{\rm Tot}_{R_{\rm e}/2}/(R_{\rm e}/1\,{\rm kpc})^2)$ which compares to the gradient of $\mathrm{d}\alpha/\mathrm{d}\log[M^{\rm Tot}_{R_{\rm e}/2}/(R_{\rm e}/1\,{\rm kpc})^2] = 0.85 \pm 0.19$ for the SLACS lenses as measured by Auger et al. (2010b).

[3] Here, we have taken a slice through the four-dimensional plane that Sonnenfeld et al. fit to the density profile slope by assuming a redshift of 0.3 and a stellar mass of $\log(M_*/{\rm M}_\odot) = 11.5$.

5 DISCUSSION

As the preceding section has shown, in all observational diagnostics and trends we have considered, bar the correlation between $f_{\rm DM}$ and $R_{\rm e}$, the H-ATLAS lenses are more similar to the SL2S lenses than those of SLACS. This is perhaps not surprising when one considers the following characteristic median values expressed in order SLACS, SL2S, H-ATLAS: $\widetilde{R}_{\rm e} \simeq 8$, 5, 3 kpc; $\widetilde{M}_{*} \simeq 10^{11.6}$, $10^{11.5}$, $10^{11.2}\,{\rm M}_{\odot}$; $\widetilde{M}^{\rm Tot}_{R_{\rm e}/2} \simeq 10^{11.2}$, $10^{11.0}$, $10^{10.8}\,{\rm M}_{\odot}$. It appears to be the case therefore, at least in the SDP data, that the H-ATLAS lenses populate the low-mass tail of the SL2S lens sample.

Despite these obvious differences and despite our very small sample of lenses at present, we still detect many of the correlations found in the various other aforementioned studies. These studies have taken care to ensure that the trends they detect are not the result of selection biases or systematic effects. In a similar vein, a possible systematic effect to be considered when comparing our results with these is that our lensing analysis does not incorporate any additional constraints from dynamical measurements. This means that the slope is measured in the vicinity of the Einstein ring, whereas in analyses using lensing and dynamics, the average slope interior to the Einstein ring is measured. Therefore, a change in slope with radius could potentially introduce a systematic offset in the slopes determined in the present work with respect to those from lensing and dynamics. However, as previously mentioned, on the scales probed by strong lensing, the slope appears not to exhibit any significant dependence on radius since there is no apparent trend in slope with the ratio of Einstein radius to effective radius (Koopmans et al. 2006; Ruff et al. 2011).

This is related to the effect reported in Ruff et al. (2011) and Bolton et al. (2012) that the ratio of the Einstein radius to the lens galaxy's effective radius increases with increasing lens redshift. This is due to the redshift dependence of the angular diameter distance ratios which govern the lensing geometry and the fact that a fixed physical size reduces in angular extent with increasing redshift (at least out to the lens redshifts in this work). This has the result that as redshift is increased, the density profile is measured by our lensing-only analysis at a radius which is an increasing multiple of the effective radius. A change in slope with radius would therefore mimic a change in slope with redshift. However, in addition to the observational evidence that the slope is not seen to depend on radius on strong lensing scales, on much larger scales, the slope is expected to steepen with increasing radius according to simulations and the requirement that the total halo mass converges. Therefore, even if this steepening were to influence our slope measurements, our detection of the rate at which slopes become less steep with increasing redshift must be a lower limit to the intrinsic rate.

In terms of a physical interpretation of observed variations in the density profile slope, the picture is somewhat unclear. Simulations by Dubois et al. (2013) reproduce the observed steepening with decreasing redshift and find that feedback from active galactic nuclei (AGN) modifies the slope. This work indicates that AGN feedback is required to reproduce the near-isothermal profiles (i.e. $\alpha \simeq 2$) observed in low-redshift early-type galaxies. However, the simulations of Remus et al. (2013) indicate that whilst a combination of dry minor and major mergers produce near-isothermality at low redshifts, the slopes are significantly steeper at higher redshift. Confounding this is the simulation work of Nipoti, Treu & Bolton (2009) which shows that the total mass profile of early types is not modified at all by dry mergers.

Turning to the projected dark matter fraction within half the effective radius, $f_{\rm DM}$, Dubois et al. (2013) claim that AGN feedback is required to reproduce the observed fractions and that without it, the fraction of stellar mass is too high. The SLACS work reports a 5σ detection of increasing $f_{\rm DM}$ with effective radius. This compares to our marginal detection (2.3σ) and a null detection in the SL2S lenses. If this trend is real, an obvious interpretation might be that star formation efficiency reduces as halo mass increases. Another possibility is presented by Nipoti et al. (2009) who predict that the fraction of dark matter within the effective radius increases as a result of mergers.

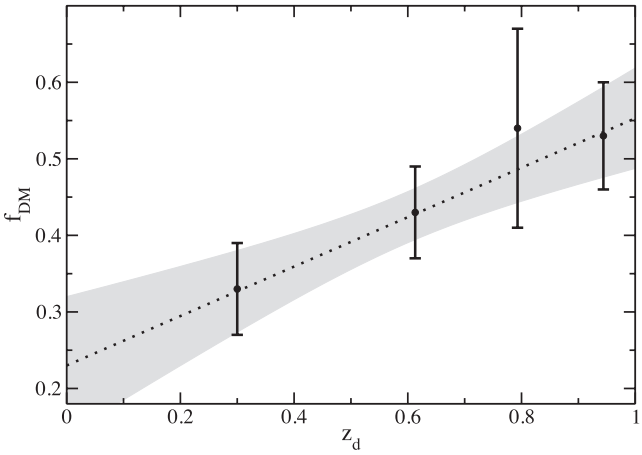

Figure 5. Variation of the fraction of dark matter within half the effective radius, $f_{\rm DM}$, for a Salpeter IMF with redshift. The grey shading depicts the 1σ error region for the straight line fit.

Instead of investigating how $f_{\rm DM}$ varies with effective radius, an alternative is to test whether $f_{\rm DM}$ changes with redshift since this is another diagnostic which can be provided by simulations.

Fig. 5 shows this plot for the H-ATLAS lenses (excluding J091305.0−005343). We measure a straight line fit of $f_{\rm DM} = 0.23 \pm 0.09 + (0.32 \pm 0.14)z$. In comparison, the simulations of Dubois et al. (2013) predict that the fraction of dark matter within 10 per cent of the virial radius decreases with increasing redshift when AGN feedback is present, or, that this fraction remains constant with redshift if AGN feedback is not present. If the fraction of dark matter within 10 per cent of the virial radius scales in the same way as $f_{\rm DM}$, then this is in contrast to our findings. However, since $f_{\rm DM}$ depends on the size of the stellar component and the virial radius effectively does not, there is still the possibility that the two results are consistent if the stellar mass increases in spatial extent relative to the dark matter with increasing redshift.

Important clues also come from comparing the morphology of the visible component of the lenses with that of the dark matter halo. We find significant discrepancies in the alignment and ellipticity between the stellar component and the total mass in some lenses. The discrepancies are consistent with what has been measured in the SL2S sample but larger than those found in SLACS. This may be a combination of the fact that both the H-ATLAS and SL2S lenses have a higher average ratio of Einstein radius to effective radius than the SLACS lenses and that the baryonic morphology correlates less strongly with that of the dark matter at larger radii (e.g. Bett et al. 2010; Skibba & Macciò 2011). In order to proceed with a more robust interpretation of these findings, more input is required from simulation work although as we previously discussed, present indications are that such large morphological differences between the dark and baryonic components are to be expected.

6 SUMMARY

In this paper, we have modelled the first five strong gravitational lens systems discovered in the H-ATLAS SDP data. To directly compare with other lensing studies, we have modelled the lenses with elliptical power-law density profiles and searched for trends in the power-law slope and the fraction of dark matter contained within half the effective radius. We have found consistency with almost all existing lens analyses, although with our present sample of only five lenses, we lack high statistical significance in our measured trends. The main results of this paper are that:

(i) the slope of the power-law density profile varies with redshift according to $\alpha = 2.05 \pm 0.08 - (0.30 \pm 0.14)z$.

(ii) the H-ATLAS lenses have a mean projected dark matter fraction within half the effective radius of $f_{\rm DM} = 0.46$ with a scatter of 0.10, for a Salpeter IMF;

(iii) the dark matter fraction within half the effective radius scales with effective radius as $f_{\rm DM} = -0.01 \pm 0.20 + (1.04 \pm 0.46)\log(R_{\rm e}/1\,{\rm kpc})$;

(iv) the slope of the power-law density profile scales with effective radius as $\alpha = 2.17 \pm 0.20 - (0.70 \pm 0.47)\log(R_{\rm e}/1\,{\rm kpc})$ and with the average total surface mass density within half the effective radius, as quantified by the ratio $M^{\rm Tot}_{R_{\rm e}/2}/(R_{\rm e}/1\,{\rm kpc})^2$ as $M^{\rm Tot}_{R_{\rm e}/2}/(R_{\rm e}/1\,{\rm kpc})^2$;

(v) $f_{\rm DM}$ scales with redshift as $f_{\rm DM} = 0.23 \pm 0.09 + (0.32 \pm 0.14)z$.

The modelling in this paper used near-IR *HST* data. Whilst the *HST* provides the high-resolution imaging necessary for modelling of high-redshift lenses, not all of the H-ATLAS lensed sources will be as readily detected in the near-IR as the SDP lenses considered herein. Being submm selected systems, submm and radio interferometry is the ideal technology for obtaining the required signal to noise and image resolution. This has been demonstrated by (B13) who have used the SMA to image several tens of lenses detected by the *Herschel Space Observatory*. Atacama Large Millimetre Array (ALMA) has also been used to image some of the SPT lenses (see, for example Hezaveh et al. 2013). However, the true power of this facility will not be realized until it operates with its full complement of antennas. At this point, ALMA will begin to deliver the high signal-to-noise and high-resolution images required by source-inversion lens modelling methods, necessary for the strongest possible constraints on galaxy mass profiles. Furthermore, spectral line imaging with ALMA will open up the possibility of reconstructing lensed source velocity maps to probe the dynamics of high-redshift submm galaxies.

The H-ATLAS lens sample is very much in its infancy. As the size of the sample grows and begins to populate the $z_{\rm d} \simeq 1$ realm and beyond, constraints on the evolution of mass in galaxies will continue to strengthen.

ACKNOWLEDGEMENTS

The work in this paper is based on observations made with the NASA/ESA *Hubble Space Telescope* under the *HST* programme #12194. MN acknowledges financial support from ASI/INAF Agreement I/072/09/0 and from PRIN-INAF 2012 project: 'Looking into the dust-obscured phase of galaxy formation through cosmic zoom lenses in the Herschel Astrophysical Large Area Survey'. JGN acknowledges financial support from the Spanish Ministerio de Ciencia e Innovacion, project AYA2010-21766-C03-01, and the Spanish CSIC for a JAE-DOC fellowship, co-funded by the European Social Fund. We thank Martin Baes and Michal Michalowski for constructive comments on this paper. We would also like to thank Adam Moss for technical discussions regarding the MCMC analysis contained herein.

REFERENCES

Ade P. A. R. et al. (Planck Collaboration), 2013, A&A, preprint (arXiv:1303.5076)
Auger M. W., Treu T., Bolton A. S., Gavazzi R., Koopmans L. V. E., Marshall P. J., Bundy K., Moustakas L. A., 2009, ApJ, 705, 1099
Auger M. W., Treu T., Gavazzi R., Bolton A. S., Koopmans L. V. E., Marshall P. J., 2010a, ApJ, 721, L163
Auger M. W., Treu T., Bolton A. S., Gavazzi R., Koopmans L. V. E., Marshall P. J., Moustakas L. A., Burles S., 2010b, ApJ, 724, 511
Barnabè M., Spiniello C., Koopmans L. V. E., Trager S. C., Czoske O., Treu T., 2013, MNRAS, 436, 253
Bell E. et al., 2006, ApJ, 640, 241
Bett P., Eke V., Frenk C. S., Jenkins A., Okamoto T., 2010, MNRAS, 404, 1137
Bolton A. S., Burles S., Koopmans L. V. E., Treu T., Moustakas L. A., 2006, ApJ, 638, 703
Bolton A. S., Burles S., Koopmans L. V. E., Treu T., Gavazzi R., Moustakas L. A., Wayth R., Schlegel D. J., 2008, ApJ, 682, 964
Bolton A. S. et al., 2012, ApJ, 757, 82
Brownstein J. R. et al., 2012, ApJ, 744, 41
Bryan S. E., Kay S. T., Duffy A. R., Schaye J., Vecchia C. D., Booth C. M., 2013, MNRAS, 429, 3316
Bundy K., Ellis R. S., Conselice C. J., 2005, ApJ, 625, 621
Bundy K., Treu T., Ellis R. S., 2007, ApJ, 665, L5
Bussmann R. S. et al., 2013, ApJ, 779, 25 (B13)
Cabanac R. A. et al., 2007, A&A, 461, 813
Carlstrom J. E. et al., 2011, PASP, 123, 568
Chabrier G., 2003, PASP, 115, 763
Ciotti L., Ostriker J. P., Proga D., 2009, ApJ, 699, 89
Cole D. R., Dehnen W., Read J. I., Wilkinson M. I., 2012, MNRAS, 426, 601
Croton D. J., 2006, MNRAS, 369, 1808
Daddi E. et al., 2005, ApJ, 626, 680
de Blok W. J. G., Bosma A., 2002, A&A, 385, 816
Dubois Y., Gavazzi R., Peirani S., Silk J., 2013, MNRAS, 433, 3297
Duffy A. R., Schaye J., Kay S. T., Vecchia C. D., Battye R. A., Booth C. M., 2010, MNRAS, 405, 2161
Dutton A. A. et al., 2013, MNRAS, 428, 3183
Dye S., Warren S. J., 2005, ApJ, 623, 31
Dye S., Smail I., Swinbank A. M., Ebeling H., Edge A. C., 2007, MNRAS, 379, 308
Dye S., Evans N. W., Belokurov V., Warren S. J., Hewett P., 2008, MNRAS, 388, 384
Eales S. et al., 2010, PASP, 122, 499
Eisenstein D. J. et al., 2011, AJ, 142, 72
Gavazzi R., Treu T., Marshall P. J., Brault F., Ruff A., 2012, ApJ, 761, 170
González-Nuevo J. et al., 2012, ApJ, 749, 65
Hezaveh Y. D. et al., 2013, ApJ, 767, 132
Hilz M., Naab T., Ostriker J. P., 2013, MNRAS, 429, 2924
Hopkins P. F., Bundy K., Hernquist L., Wuyts S., Cox T. J., 2010, MNRAS, 401, 1099
Jackson N., 2007, Living Rev. Relativ., 10, 4
Kassiola A., Kovner I., 1993, ApJ, 417, 450
Khochfar S., Burkert A., 2003, ApJ, 597, 117
Koopmans L. V. E., Treu T., Bolton A. S., Burles S., Moustakas L. A., 2006, ApJ, 649, 599
Krist J. E., 1993, in Hanisch R. J., Brissenden R. J. V., Barnes J., eds, ASP Conf. Ser. Vol. 52, Astronomical Data Analysis Software and Systems II. Astron. Soc. Pac., San Francisco, p. 536
Lani C. et al., 2013, MNRAS, 435, 207
Limousin M. et al., 2010, A&A, 524, A95

Loeb A., Weiner N., 2011, Phys. Rev. Lett., 106, 1302
Lovell M. R. et al., 2012, MNRAS, 420, 2318
Maoz D., Rix H.-W., 1993, ApJ, 416, 425
Maraston C., Strömbäck G., Thomas D., Wake D. A., Nichol R. C., 2009, MNRAS, 394, 107
Negrello M. et al., 2010, Science, 330, 800
Negrello M. et al., 2014, MNRAS, in press, doi:10.1093/mnras/stu413
Newton R. D. A., Kay S. T., 2013, MNRAS, 434, 3606
Nipoti C., Treu T., Bolton A. S., 2009, ApJ, 703, 1531
Oliver S. J. et al., 2012, MNRAS, 424, 1614
Oser L., Naab T., Ostriker J. P., Johansson P. H., 2012, ApJ, 744, 63
Peng C. Y., Ho L. C., Impey C. D., Rix H.-W., 2002, AJ, 124, 266
Pilbratt G. L. et al., 2010, A&A, 518, L1
Remus R.-S., Burkert A., Dolag K., Johansson P. H., Naab T., Oser L., Thomas J., 2013, ApJ, 766, 71
Ruff A. J., Gavazzi R., Marshall P. J., Treu T., Auger M. W., Brault F., 2011, ApJ, 727, 96
Salpeter E. E., 1955, ApJ, 121, 161
Schaye J. et al., 2010, MNRAS, 402, 1536
Schneider P., Ehlers J., Falco E. E., 1992, Gravitational Lenses. Springer-Verlag, New York
Skibba R. A., Macciò A. V., 2011, MNRAS, 416, 2388
Sonnenfeld A., Treu T., Gavazzi R., Suyu S. H., Marshall P. J., Auger M. W., Nipoti C., 2013, ApJ, 777, 98
Spergel D. N., Steinhardt P. J., 2000, Phys. Rev. Lett., 84, 3760
Suyu S. H., Marshall P. J., Hobson M. P., Blandford R. D., 2006, MNRAS, 371, 983
Tewes M. et al., 2013, A&A, 556, A22
Thomas D., Maraston C., Bender R., Mendes de Oliveira C., 2005, ApJ, 621, 673
Tojeiro R. et al., 2012, MNRAS, 424, 136
Treu T., 2010, ARA&A, 48, 87
Treu T., Koopmans L. V. E., 2004, ApJ, 611, 739
Treu T., Auger M. W., Koopmans L. V. E., Gavazzi R., Marshall P. J., Bolton A. S., 2010, ApJ, 709, 1195
Treu T., Dutton A. A., Auger M. W., Marshall P. J., Bolton A. S., Brewer B. J., Koo D. C., Koopmans L. V. E., 2011, MNRAS, 417, 1601
Trujillo I. et al., 2006, MNRAS, 373, L36
van der Wel A., Bell E. F., van den Bosch F. C., Gallazzi A., Rix H.-W., 2009, ApJ, 698, 1232
van Dokkum P. G., Franx M., Fabricant D., Kelson D. D., Illingworth G. D., 1999, ApJ, 520, L95
van Dokkum P. G. et al., 2008, ApJ, 677, 5
Velander M. et al., 2014, MNRAS, 437, 2111
Vieira J. D. et al., 2013, Nature, 496, 344
Walker M. G., Combet C., Hinton J. A., Maurin D., Wilkinson M. I., 2011, ApJ, 733, L46
Wardlow J. et al., 2013, ApJ, 762, 59
Warren S. J., Dye S., 2003, ApJ, 590, 673

APPENDIX A: LENS PARAMETER CONFIDENCE PLOTS

In this appendix, we plot the confidence contours for all parameter combinations for each lens (apart from the lens position parameters x_c and y_c since we did not detect any significant offsets between the lens mass centre and the centroid of the lens galaxy light). In each plot, the contours correspond to the 1, 2 and 3σ confidence levels.

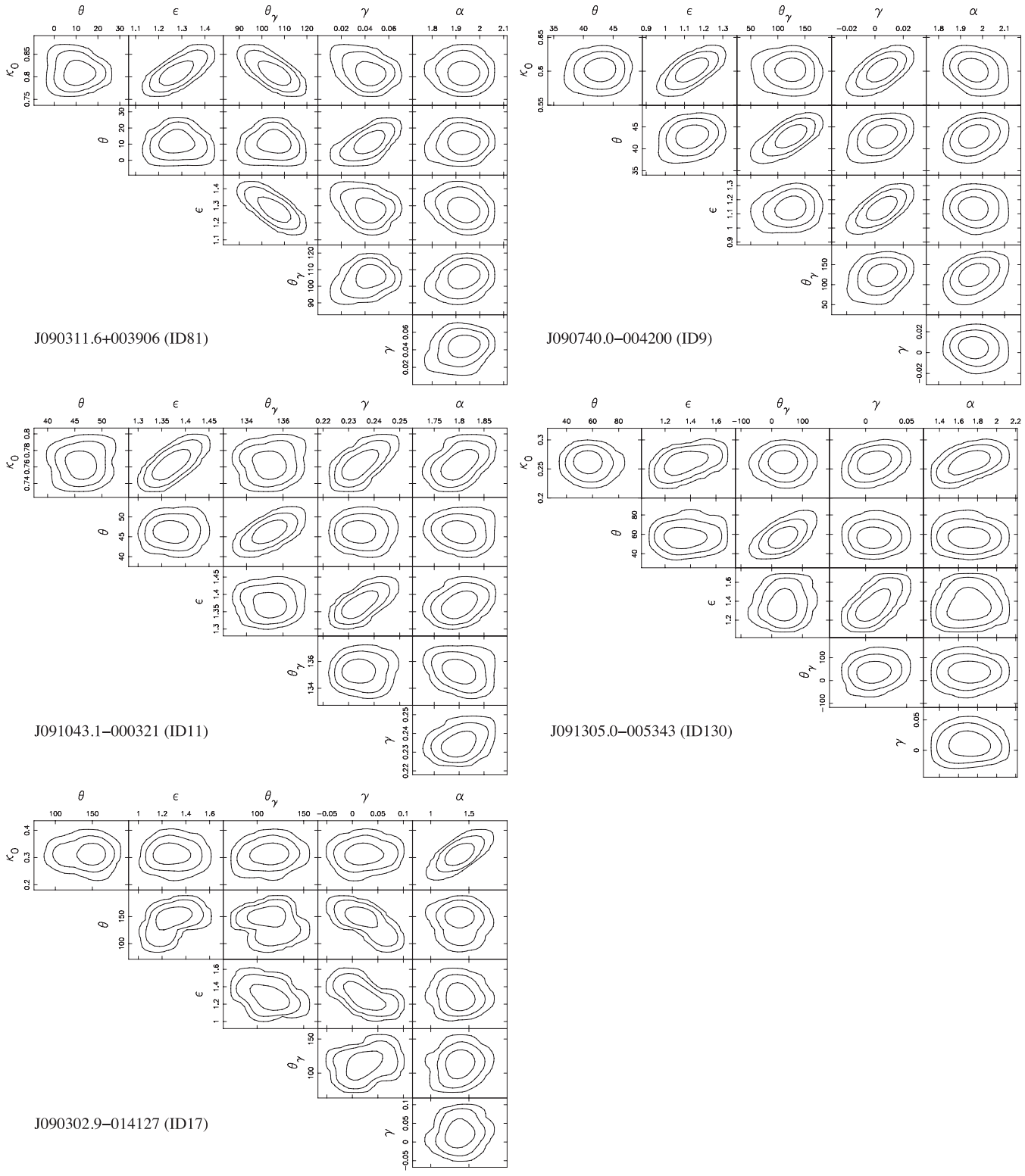

Figure A1. Parameter confidence limits. Contours show the 1, 2 and 3σ single-parameter confidence regions for all parameter combinations, excluding the position centroid of the lens.

This paper has been typeset from a TEX/LATEX file prepared by the author.